Probing atom-surface interactions from tunneling-time measurements via rotation transport on an atom chip

J-B. Gerent,[1,*] R. Veyron,[2] V. Mancois,[3,4] R. Huang,[5] E. Beraud,[5] and S. Bernon[5,†]

[1]*Department of Physics and Astronomy, Bates College, Lewiston, Maine 04240, USA*
[2]*ICFO—Institut de Ciencies Fotoniques, The Barcelona Institute of Science and Technology, Castelldefels, 08860 Barcelona, Spain*
[3]*Nanyang Quantum Hub, School of Physical and Mathematical Sciences, Nanyang Technological University, 21 Nanyang Link, Singapore 637371, Singapore*
[4]*MajuLab, International Joint Research Unit IRL 3654, CNRS, Université Côte d'Azur, Sorbonne Université, National University of Singapore, Nanyang Technological University, Singapore*
[5]*LP2N, Laboratoire Photonique, Numérique et Nanosciences, Université de Bordeaux-IOGS-CNRS:UMR 5298, rue F. Mitterrand, F-33400 Talence, France*

(Received 26 February 2026; accepted 10 August 2026; published 8 September 2026)

We propose a method to measure the interaction between an ultracold gas of neutral atoms and a surface. This solution combines an optical dipole trap reflected by the surface, a magnetic trap formed by current carrying wires embedded below the surface, and a rotation of the surface itself. It allows to adiabatically transport a ^{87}Rb Bose-Einstein condensate from few micrometers to few hundred nanometers of the surface. At such distances, atom-surface interaction strongly affects the trapping potential, causing an increase of the tunneling rate toward the surface. In this paper, we show that the measurement of the lifetime of the cloud and its comparison to a tunneling model will allow to extract the Casimir-Polder force coefficient in the retarded regime (c_4). Our model includes noise-induced heating, calibration biases of experimentally controlled parameters, and accuracy of the atom lifetime measurement. Using typical trapping parameters and experimental uncertainties, we numerically estimate the relative uncertainty of c_4 to be 10%. This method can be implemented with any atomic species that can be magnetically and optically trapped.

DOI: 10.1103/qcq3-c6ph

I. INTRODUCTION

Ultracold atoms trapped in optical or magnetic potentials are the building blocks of the emerging field of atomtronics [1]. Controlling atoms in the vicinity of surfaces enables strong atom-light coupling, allowing to explore quantum regimes where intricate quantum correlations [2,3] and strongly correlated phases [4] can be achieved. Reaching an exhaustive control of atomic states and dynamics requires a precise knowledge of atom-surface interactions. Among these, the van der Waals (vdW) interaction [5,6] that arises from the interaction between a ground-state atom and a surface has attracted lots of theoretical interest with intriguing predictions for structured surfaces [7], excited state [8], tunability of multilayers surfaces [9], or quantum reflection-induced levitation [10].

In this field, theoretical predictions are strongly ahead of experimental realizations that mainly focus on measuring the strength of the interaction and its dependence on temperature [11]. The atom-surface interaction potential is governed by an inverse power law $U_{\mathrm{vdW}} = -c_\alpha/z^\alpha$, where c_α is the interaction strength coefficient and z is the atom-surface distance. The exponent α has been derived theoretically for various distance range z. At short distance, the interaction energy scales as $\alpha = 3$ [6] (Lennard-Jones or LJ regime), while it scales as $\alpha = 4$ at large distance (Casimir-Polder or CP regime) where retardation effects need to be taken into account [12]. The crossover between the two regimes is around $z \approx \lambda/(2\pi)$, where λ is the wavelength of the dominant atomic transition involving the ground state.

The experiments, mostly concerned with determining the interaction strength, adopt a static, dynamic, or statistical strategy. Static measurements extract the coefficient from a local measurement of the atomic properties. This was, for example, realized by measuring the change of center-of-mass oscillation frequency of a Bose-Einstein condensate (BEC) in the vicinity of a surface [13] or using matter-wave interferometry techniques in a one-dimensional (1D) lattice [14]. While achieving extreme measurement sensitivity, both methods were limited, by the size of the atomic sample, to probe the interaction at large distances ($z > 1$ µm, CP regime). On the other hand, dynamic measurements extract the interaction strength from the study of a cold atom cloud scattered by the surface potential. Typical surface geometries that have been probed include planar surfaces using either optical

*Contact author: jean-baptiste.gerent@institutoptique.fr
†Contact author: simon.bernon@institutoptique.fr

barrier reflection [15] or quantum reflection principles [16], and subwavelength periodically patterned surfaces inducing diffraction of the reflected [17,18] or transmitted [19–22] matter wave. At short distances, the vdW regime has mainly been probed by direct spectroscopy for hydrogen atoms adsorbed on the surface of liquid helium [23] or by frequency selective reflection spectroscopy [24–26] of alkali atoms in a glass cell. In reflection spectroscopy, atoms from a vapor are probed by the evanescent field of a total internal reflection, thus limiting the probed volume to only a fraction of the optical wavelength.

In this paper, we propose to probe atom-surface interactions in the CP regime by adiabatically and continuously transporting a cloud of ultracold atoms toward a surface. Adiabatic transport typically involves magnetic interaction [27,28] or far off-resonance electric dipole interaction driven by an optical field at wavelength λ_0 [29,30]. As in Ref. [31], our solution combines both approaches, enabling a continuous control over the atom-surface distances from few λ_0 down to $\lambda_0/4$. It is therefore well suited to study atom-surface interactions in the CP regime. It is worth mentioning that our method, which we refer to as *rotation transport*, could be combined at large distance with an adiabatic loading from a magnetic chip trap [32], and at short distance with doubly dressed states trapping [33,34], allowing to reach nanometric atom-surface distances. We propose here to use this rotation transport to bring a cloud of atoms close to a surface to probe the attractive force of the surface on the atoms. The method relies on measuring the lifetime of the cloud when the tunneling time toward surface-bonded states becomes predominant [35–37]. We present in Fig. 1(a) sketch of our method: We plot in panel (c) 1D cuts along z of the total (plain line) and optical (dashed line) potential at the trap center (x_0, y_0). A wave packet (in green) can, in such potential, tunnel toward other lattice sites (increasing z) or toward the surface (at $z = 0$). The attractive CP force will mainly decrease the barrier height toward the surface, leading to a shorter tunneling time constant τ_t toward the surface. The dependency of the tunneling time with the surface-dependent CP coefficient and with well-controlled and tunable experimental parameters (surface angle and optical power) is the core of our measurement method.

The paper is organized as follows: First, we introduce the rotation transport method in Sec. II with no atom-surface interactions. Then, we present numerical simulation results in Sec. III with general trap parameters in Sec. III A and show in Sec. III B that CP forces need to be taken into account. By doing so, we highlight how the rotation transport method can be used to perform a measurement of surface-atom interaction coefficients. Furthermore, we discuss the experimental implementation of our method in Sec. IV. We derive in Sec. IV A the relative precision achievable in typical conditions. Finally, we discuss in Sec. IV B additional uncertainties and loss terms such as three-body and background losses, transport adiabaticity, adsorbate induced and patch electric fields, refractive index uncertainty, and Johnson noise.

II. ROTATION TRANSPORT METHOD

In this section, we present the rotation transport method and introduce how it can be used to precisely measure the c_4 coefficient. The transport is done by rotating a surface

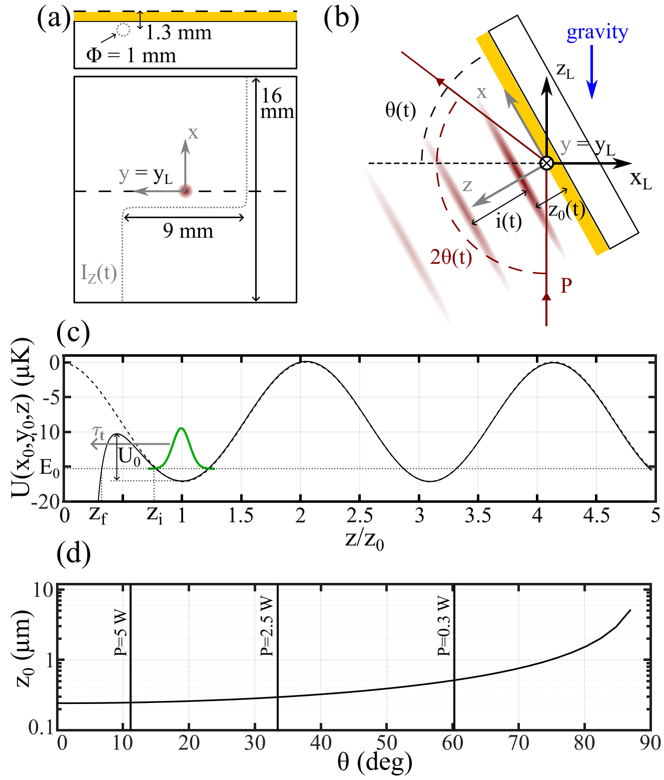

FIG. 1. (a) Drawing of the chip's copper substrate: (top) side view and (bottom) top view. A gold mirror (yellow) is glued on top of the substrate. The rotating axis of the chip (dashed black line, along $y = y_L$) aligns with the top surface of the chip above the mirror. A Z-shaped wire (gray dotted line) carrying a current $I_Z(t)$ is embedded in a groove between the mirror and the substrate. A 1064 nm laser (red fading circle) is reflected by the mirror at the center of the chip (origin of both frames of reference). (b) Interference fringes [interfringe $i(t)$] are produced at a distance $z_0(t)$ from the chip by reflecting the laser beam (fixed, propagating along $+z_L$) while rotating the chip, resulting in a time-dependent angle of incidence $\theta(t)$. (c) 1D cut of the total (plain line) and optical (dashed line) potential in the perpendicular (z) direction at $\theta = 65^\circ$. The wave function (green) can tunnel toward the surface at $z = 0$ with a timescale τ_t. (d) Semilog plot of the trap center position z_0 as a function of θ in the absence of CP forces. The vertical lines represent the lowest trapping angle one can reach when including CP forces with $c_4 = 2.1 \times 10^{-55}$ J m^4 for different optical powers P.

on which a fixed laser beam (propagating along $+z_L$), acting as a dipole trap (DT) [29,30] is reflected. We define a frame of reference (FoR) (x, y, z) associated with the surface [see Figs. 1(a) and 1(b), in gray] rotated by the angle $\theta(t)$ compared to the fixed laboratory (in black) FoR (x_L, y_L, z_L). The reflecting layer is integrated on an atom chip [38] with a Z-shaped current-carrying wire of millimeter size, producing a magnetic gradient, which compensates gravity along one of the weakly trapping transverse direction (x).

We now concentrate on the DT generated by the reflected laser. The total intensity is derived in Refs. [39,40]. We focus here on the simplified case of an incident field polarized along y (transverse electric, TE). In this case, the generalized complex Fresnel coefficient modulus is almost constant as a function of the incidence angle [$|\rho_{TE}(\theta)| \simeq 1$]. The intensity (including the reflection) can be written as

$$I(x, y, z) = \frac{2P}{\pi w_0^2}\left(e^{-2r_i^2/w_0^2} + e^{-2r_r^2/w_0^2} + 2e^{-(r_i^2+r_r^2)/w_0^2}\cos\left(\frac{4\pi}{\lambda_0} z\cos\theta + \phi_{\mathrm{TE}}(\theta)\right)\right), \tag{1}$$

where $r_i^2 = (x\cos(\theta) - z\sin(\theta))^2 + y^2$ [resp. $r_r^2 = (x\cos(\theta) + z\sin(\theta))^2 + y^2$] is the radial distance from (x, y, z) to the propagation axis of the incident (resp. reflected) beam, $\phi_{\mathrm{TE}}(\theta)$ is the angle-dependent phase of the Fresnel coefficient, P the optical power of the incident beam, and $\lambda_0 = 1064$ nm the dipole trap wavelength. The above intensity presents evenly spaced fringes of period $i(t)$ in the longitudinal direction (z). The transverse profile depends on the incident beam profile that is, assumed Gaussian, of waist $w_0 = 150$ μm throughout this paper. The first fringe position $r_0 = (x_0, y_0, z_0)$ is computed numerically. For surfaces with a complex index of refraction, the incident electric field slightly penetrates the surface before being reflected, leading to an angle dependence of the reflected electric field phase [$\phi_{\mathrm{TE}}(\theta)$]. Albeit this effect, the first fringe position is given with a good approximation in the transverse direction by

$$z_0(\theta) \simeq \frac{\lambda_0}{4\cos\theta}. \tag{2}$$

As illustrated in Fig. 1(d), z_0 can be reduced by decreasing the incidence angle, thus transporting atoms, previously loaded into one of the fringes, toward the chip.

The total potential can be written as

$$\begin{aligned} U(x, y, z) &= U_{\mathrm{mag}}(x, y, z) + U_{\mathrm{grav}}(x, z) \\ &\quad + U_{\mathrm{opt}}(x, y, z) + U_{\mathrm{CP}}(z) \\ &= \mu_B|B(x, y, z)| \\ &\quad + mg(x\sin\theta - z\cos\theta) \\ &\quad + C_{\mathrm{dip}} I(x, y, z) - \frac{c_4}{z^4}, \end{aligned} \tag{3}$$

where C_{dip} is a parameter proportional to the atomic polarizability and fully defined in Eqs. (10) and (19) in Ref. [41]. For a linearly polarized beam and for ^{87}Rb atoms where we consider both transitions of the D-line doublet $5^2\mathrm{S}_{1/2} \rightarrow 5^2\mathrm{P}_{1/2}, 5^2\mathrm{P}_{3/2}$, it reads

$$C_{\mathrm{dip}} = \frac{\pi c^2\Gamma_2}{\omega_2^3}\left(\frac{1}{\omega-\omega_2} - \frac{1}{\omega+\omega_2}\right) + \frac{\pi c^2\Gamma_1}{2\omega_1^3}\left(\frac{1}{\omega-\omega_1} - \frac{1}{\omega+\omega_1}\right), \tag{4}$$

with c the speed of light, ω the dressing laser angular frequency, ω_1 (resp. ω_2) the frequency between $|5^2\mathrm{S}_{1/2}, F = 2\rangle$ and $|5^2\mathrm{P}_{1/2}, F = 2\rangle$ (resp. $|5^2\mathrm{P}_{3/2}, F = 2\rangle$), and Γ_i ($i = \{1, 2\}$) the natural linewidth of the transitions. At a fixed angle, decreasing the optical power will decrease the tunneling time, eventually leading to a case where atoms are not trapped anymore. To indicate the different atom-surface distances that can be reached, this threshold is represented in Fig. 1(d) as vertical black lines, each annotated with the corresponding optical power. Unless specified, the default value of the CP coefficient is taken as the average of various theoretical values [17,42–47] (considering flat surfaces, both dielectric and metalic) found in the literature as $c_4 = 2.1 \times 10^{-55}$ J m^4.

By measuring the atomic cloud lifetime (when limited by tunnel losses), which depends on the first fringe barrier height, one can extract the value of the c_4 coefficient. Adjusting the barrier height (U_0) can be done either by varying the incidence angle or the optical power, which are two experimentally well-controlled parameters.

III. NUMERICAL MODEL

We present in this section the results of numerical calculations. In Sec. III A, we focus on the case without CP forces, presenting the shapes, frequencies, and depth of the trap produced. Then, we show in Sec. III B how the c_4 coefficient can be determined by measuring the lifetime of atoms trapped with the method presented in Sec. II.

A. Achievable trap parameters

The position of the minimum in 3D is numerically computed using the total potential defined in Eq. (3). In the following, we consider a cloud of ^{87}Rb atoms prepared in $|5^2\mathrm{S}_{1/2}, F = 2, \mathrm{m}_F = 2\rangle$ for which the s-wave scattering length is $a_0 = 5$ nm. The complex refractive index (Ref. [40], p. 249) used to compute the reflection of the electric field on the surface is $n = \tilde{n} - \kappa i = 0.247\,89 - 7.3057i$ [48]. We plot in Fig. 2(a) 1D cuts of the potential in the transverse directions (x and y) for $\theta = 65^\circ$ in the absence of CP forces. Dashed lines represent solely the optical potential (U_{opt}). It shows a Gaussian profile elongated in the x direction by the grazing incidence. The current $I_Z(\theta)$ in the Z wire is computed numerically to maintain the trap center at $x = 0$. In practice, it mostly comes down to compensate the gravity sag along x. A $\sin(\theta)$ law is therefore a good approximation for the change of current I_Z with at most 1% deviation from the exact calculation. This difference is explained by the fact that the magnetic field generated by a wire is not a pure gradient as required to perfectly compensate gravity but includes higher-order terms that cause the asymmetry of $U(x)$ at $|x| > 250$ μm. To represent a realistic experimental implementation, we have chosen for our simulations a Z-shape trapping geometry that breaks the translational symmetry along y. Compensating for gravity along x therefore leads to a residual magnetic gradient along y as shown by the tilt of $U(y)$ (gray plain line—right axis).

As shown in Fig. 1(d), reducing the incidence angle (θ) brings the first fringe closer to the surface but also compresses the trap by increasing the trapping frequency in the x (resp. z) direction, as shown in Fig. 2(b) [resp. panel (c)]. To trustfully extract a trap curvature from this slightly nonharmonic potential, the trap frequencies are computed with a 1D fit at the bottom of the potential over a length scale being twice the Thomas-Fermi radius along x and y or twice the quantum harmonic oscillator (QHO) length along z. The cloud is strongly confined along z such that its size in this direction is reduced and given by the QHO length $a_{\mathrm{QHO}} = \sqrt{\hbar/(2\pi\nu_z m)} \approx 50$ nm. The wave packet is thus much smaller than the DT wavelength

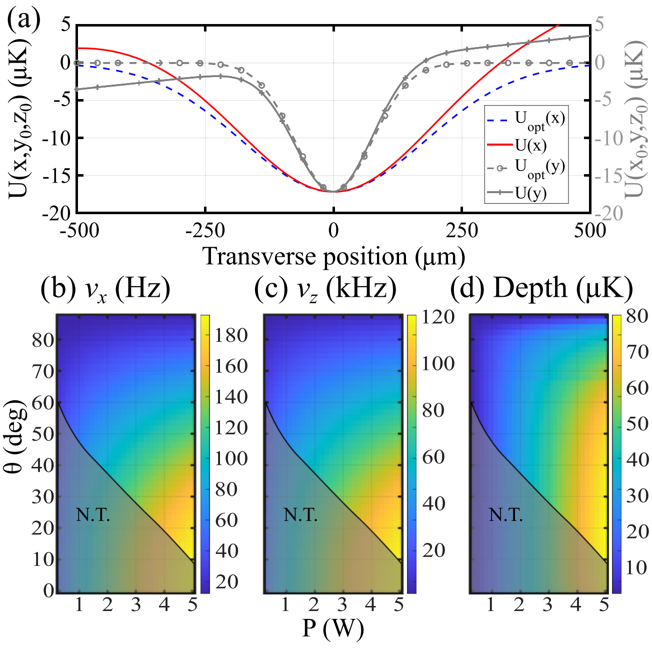

FIG. 2. (a) 1D cuts of the potential in the transverse directions. Along x at (y_0, z_0) (left axis, colors, no markers). Along y at (x_0, z_0) (right axis, gray, with markers). 2D maps of trap parameters in the absence of CP forces, as a function of both P and θ [panel (b)] [resp. panel (c)]. Trap frequency in the x (resp. z) direction. (d) Barrier height (U_0). The shaded area below the black line annotated N.T. (no trap) corresponds to a nontrapping configuration when including CP forces with $c_4 = 2.1 \times 10^{-55}\,\mathrm{J\,m^4}$. These parameters are achievable nevertheless in the second fringe where the CP force induces very little modification and could be neglected.

λ_0, allowing to selectively probe CP force spatially, down to the minimum distance of $\lambda_0/4$ [see Eq. (2)].

We plot in Fig. 2(d) the trap depth calculated as the minimum of the potential depth in the x and y directions and the barrier height in the z direction. 2D maps of Fig. 2 are annotated with a black line labeled N.T., below which (gray shaded area) the barrier height U_0 is lower than the single particule energy E_0 [see Fig. 1(c)] when including CP force with $c_4 = 2.1 \times 10^{-55}\,\mathrm{J\,m^4}$. The tunelling rate increases strongly close to this N.T. region. In the next section, we show that this strong increase of the tunneling can be used to get a precise measurement of the c_4 coefficient.

B. Sensitivity on the CP coefficients

In the previous section, we presented general trap parameters as a function of the optical power and incidence angle. Including the CP force in the calculation of the potential energy [Eq. (3)] modifies the trap profile by reducing the barrier height and shape of the first fringe toward the surface. In the regime where the atomic cloud lifetime τ is limited by tunneling through this barrier, the c_4 coefficient can be inferred by measuring τ. This regime is achieved when both the technical source of atom loss (see Sec. IV B) and the inelastic three-body losses (τ_{3b}) (see Fig. 4) can be neglected with respect to the tunneling dynamics. The tunneling time is derived in the Wentzel-Kramers-Brillouin (WKB) approximation [49]. The

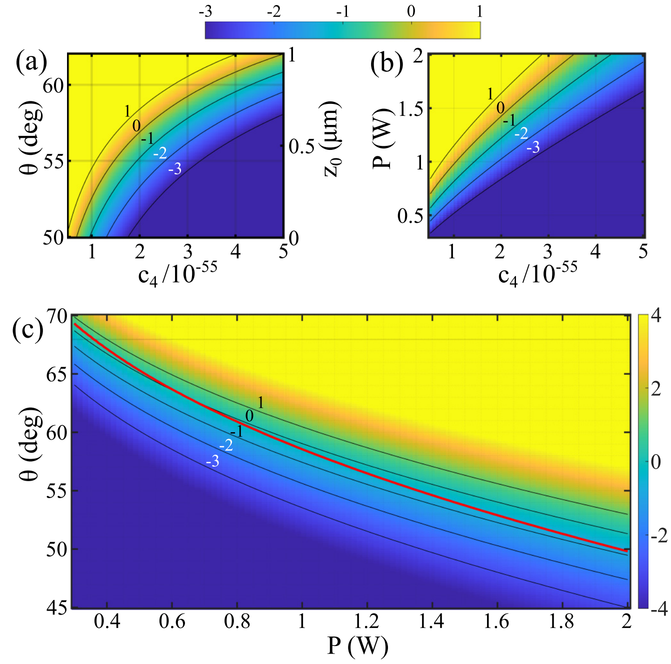

FIG. 3. 2D maps of the tunneling time, $\log_{10}(\tau_t)$, limited by the tunneling time toward the surface when including CP forces. Contour lines of annotated values are plotted in black. (a), (b) Share the same colormap (on top). They are computed at $P = 1.2\,\mathrm{W}$ for panel (a) and $\theta = 55^\circ$ for panel (b). The y axis for panel (a) [resp. (b)] is θ (resp. P). The right y axis in panel (a) shows the equivalent trap center position z_0. (c) 2D map as a function of P and θ for $c_4 = 2.1 \times 10^{-55}\,\mathrm{J\,m^4}$. The red line corresponds to $\tau_t = \tau_{3b}$.

probability for an atom to tunnel is given by

$$P_t = \frac{4}{e^{2\gamma}(1 - e^{-2\gamma})^2}, \tag{5}$$

with $\gamma = \frac{1}{\hbar}\int_{z_i}^{z_f} \sqrt{2m|U(z') - E_0|}dz'$, where E_0 is the single particule energy, z_i and z_f are the positions at which $U(z) = E_0$ [see Fig. 1(c)]. The tunneling time is then given by

$$\tau_t = \frac{1}{P_t \nu_z}. \tag{6}$$

We calculated E_0 as the energy of the ground state of a 1D QHO along z. Beyond the harmonic approximation, numerically solving the stationary Schrödinger equation using the numerical potential only induces a relative correction of $\Delta E_0/E_0 \approx 10^{-2}$ for $\tau_t > 100$ ms. The WKB approximation is then valid for tunneling time above 10 ms with a relative correction $\Delta E_0/E_0 \approx 5 \times 10^{-2}$. Over the range of our numerical simulations, the mean chemical potential satisfies $\mu < |E_0|/2, U_0/2$, justifying the treatment of the cloud as a noninteracting BEC. To reach a quantitative comparison with the experiment, the effect of interactions could be further included in the model. If this effect appears experimentally limiting, the interaction energy could be reduced by lowering the atom number.

In Fig. 3, we plot 2D maps of $\log_{10}(\tau_t)$ as a function of c_4 and the incidence angle (resp. the optical power) in panel (a) [resp. panel (b)]. We scan in panel (c) both the optical power and the angle for a fixed value of $c_4 = 2.1 \times 10^{-55}\,\mathrm{J\,m^4}$. The

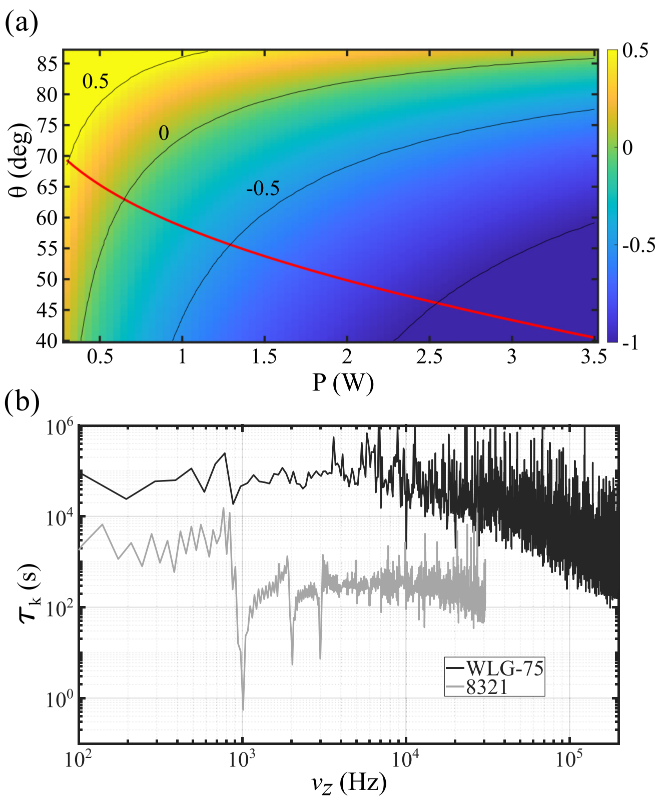

FIG. 4. (a) 2D map of the three-body recombination time $[\log_{10}(\tau_{3b})]$ as a function of P and θ. Contour lines of annotated values are plotted in black. The red line corresponds to $\tau_{3b} = \tau_t$. (b) Fluctuation-limited lifetime (τ_k) as a function of the trapping frequency (ν_z). The black curve is for a continuous rotation motor (Teckceleo). The gray curve is for a stepper motor (new focus), driven at 2 kHz.

red line corresponds to $\tau_t = \tau_{3b}$ as defined in Sec. IV B and calculated here for $N = 2 \times 10^4$ ^{87}Rb atoms in a pure BEC state. The tunneling limited regime is therefore reached for $\tau_t \ll \tau_{3b}$. We see in this figure that τ_t depends both on P, θ, and c_4, and is strictly monotonous with c_4 for fixed values of P and θ. In theory, if P and θ are absolutely known, a single measurement of the trap lifetime would determine c_4 with no ambiguity. In this case, the strong sensitivity of τ_t with c_4 will help determine c_4 precisely. However, uncertainties on (P, θ, τ) will affect the final uncertainty on the exctracted value of c_4.

Formally, we introduce a numerical function that truthfully represents c_4 as $c_4^{\mathrm{n}} = c_4^{\mathrm{n}}(\tau, \theta, P)$. The c_4^{exp} coefficient measured experimentally can be written as $c_4^{\mathrm{exp}} = c_4^{\mathrm{n}} + \delta c_4$, where δc_4 is the uncertainty on the measurement of the actual c_4^{n} coefficient.

Within this formalism, the sensitivity of the c_4^{n} coefficient with respect to θ (or one of the other parameters) can be numerically derived at constant τ_t and P using a variational approach.

Since the slope of vertical cuts of Figs. 3(a) and 3(b) (at constant c_4^{n}) depends on the value of c_4^{n}, measuring the lifetime while scanning either θ or P allows to go beyond this single shot method and circumvent systematic errors on the experimental parameters, as detailed in Appendix A. The independence of c_4 with respect to z can be verified by repeated measurement at different z_0 by scanning θ (and possibly adjusting P to keep the lifetime in the correct range). Using these curves, the sensitivity can be extracted with the variational approach mentioned above. In Sec. IV A, we give the expected sensibility for a realistic experimental implementation.

IV. DISCUSSION ON EXPERIMENTAL IMPLEMENTATION

In this section, we discuss the experimental implementation of our method. We first evaluate the uncertainty on the CP coefficient based on typical uncertainties of experimental parameters such as the beam waist, the incidence angle, the optical power, and the wire current. We then discuss the role and expected consequences of alternative physical effects such as three-body losses, transport adiabaticity, adsorbate induced and patch electric fields, background losses, refractive index uncertainty, and Johnson noise.

A. Precision on the CP coefficient

In this section, we set an upper bound on our c_4 measurement precision. For this, we measure experimental uncertainties of the parameters (θ, P, w_0, I_Z) included in our model [see Eq. (3)] and consider typically achieved experimental measurement precision of the atomic cloud lifetime to extrapolate a typical uncertainty on c_4 for the one shot measurement.

Assuming small and uncorrelated fluctuations of experimental quantities (τ) and variables (P, θ), the relative standard deviation is given by

$$\frac{\delta c_4}{c_4^{\mathrm{n}}} = \sqrt{\epsilon_\theta^2 + \epsilon_P^2 + \epsilon_\tau^2}$$

$$= \sqrt{\left(\frac{\partial c_4^{\mathrm{n}}}{\partial \theta}\frac{\delta\theta}{c_4^{\mathrm{n}}}\right)^2 + \left(\frac{\partial c_4^{\mathrm{n}}}{\partial P}\frac{\delta P}{c_4^{\mathrm{n}}}\right)^2 + \left(\frac{\partial c_4^{\mathrm{n}}}{\partial \tau}\frac{\delta \tau}{c_4^{\mathrm{n}}}\right)^2}. \quad (7)$$

Every experimental parameter can be decomposed as its true value (θ_0), a systematic error (θ_{syst}), and a statistical error ($\delta\theta$): $\theta = \theta_0 + \theta_{\mathrm{syst}} + \delta\theta$.

To experimentally rotate the surface, we consider using a continuous-wave motor (details in Sec. IV B). The optically encoded angular position and the closed-loop control system results in an uncertainty of $\delta\theta = 273$ μrad. By retroreflecting the beam, absolute calibration of the angle of the beam with respect to the surface can be easily reduced to less than $\theta_{\mathrm{syst}} = 150$ μrad. The maximum error we consider here is then $\theta_{\mathrm{syst}} + \delta\theta = 423$ μrad. The tunneling time depends on the barrier height, which is experimentally set by the optical intensity $I \propto P/w_0^2$. To first order, fluctuations of the intensity can be treated as effective fluctuations of the optical power. Uncertainty on the optical power is experimentally limited by the absolute calibration of optical detectors. A standard calibration uncertainty given by the manufacturer for [50] is $(P_{\mathrm{syst}} + \delta P)/P_0 = 6 \times 10^{-2}$. Small fluctuations of the waist are experimentally equivalent to power fluctuations. Using forced oscillations [39,51], the *in situ* dipole trap waist can be measured with a relative precision of $\delta w_0/w_0 = 4 \times 10^{-3}$. This is equivalent to a power fluctuation of $\delta\tilde{P}/P = 2\delta\omega_0/\omega_0 = 8 \times 10^{-3}$, the square of which is negligible compared to $(\delta P/P)^2$. The total uncertainty is then $\delta P/P = 6 \times 10^{-2}$.

We present here upper bounds on the different sensitivities we studied numerically, subject to optimization depending on the expected value of c_4. We consider an experimental implementation centered around the parameters: $P = 0.5\,\mathrm{W}$, $w_0 = 150\ \mu\mathrm{m}$, $\theta = 55^\circ$. For $\theta \in [52, 75]^\circ$ and $\tau_t \in [10^{-3}, 10^{-2}]\,\mathrm{s}$, the relative error contribution from angle uncertainty is $\epsilon_\theta < 20 \times 423 \times 10^{-6} = 10^{-3}$. At $\theta = 55^\circ$, the contribution from the optical power ($P \in [0.3, 2]\,\mathrm{W}$) is $\epsilon_P < 10^{-1}$. We have observed numerically that $\frac{\partial c_4^n}{\partial \tau}\frac{\tau}{c_4} \approx 0.1$ is mostly independent of τ. Thus, the contribution from the lifetime is 10 times smaller than the relative error on the lifetime ($\epsilon_\tau = \frac{\partial c_4^n}{\partial \tau}\frac{\tau}{c_4}\frac{\delta\tau}{\tau} < 0.1\frac{\delta\tau}{\tau}$) and can be statistically reduced. Even for $\frac{\delta\tau}{\tau} = 0.1$, the total uncertainty would still mainly come from ϵ_P. An error on the current in the wire or on the calibration of the background magnetic field, corresponding to an imperfect cancellation of gravity, impacts the tunneling time. For the parameters of Fig. 3(c), an offset of 10 mA (around 10 mG) induces a relative error $\epsilon_\tau < 2 \times 10^{-4}$. A power calibration from NIST [52,53] would yield an uncertainty at 1064 nm of $\delta P/P < 2 \times 10^{-3}$. This reduces the relative error down to $\frac{\delta c_4}{c_4^n} = 1.7 \times 10^{-2}$, where all uncertainties have comparable contributions. We emphasize that measuring the lifetime while scanning one of the parameters allows to be insensitive to systematic errors and could further reduce the uncertainty.

B. Additional uncertainties and loss mechanism

In this section, we discuss how additional uncertainties and loss terms (three-body losses, transport adiabaticity, adsorbate fields, background losses, refractive index uncertainty, and Johnson noise) affect the lifetime measurement and therefore our estimate of c_4. Transport adiabaticity (ability to transport an initial cloud without excitations or significant atom losses) is critical since the tunneling time depends on the trapped cloud energy (E_0).

Three-body losses. Experimentally, the inelastic three-body collision rate increases during the rotation because the change in the trap frequencies [see Figs. 2(b) and 2(c)] leads to the increase of the atomic density. We consider a BEC with 2×10^4 atoms and plot a 2D map in Fig. 4(a) of the associated time $\tau_{3b} = 1/(5.8 \times 10^{-30} \times n_0^2)$ s [54], where n_0 is the atomic density in at cm^{-3}.

To avoid this limitation, experiments should be conducted in a regime where $\tau_t \ll \tau_{3b}$, indicated by the red limit in Fig. 4(a).

Adiabatic transport. Our model considers that every particle of the cloud is in the ground state of an ideal QHO. Under this asumption, we can exclude anharmonic couplings, which would mostly impact excited states by hybridizing them and would require to account for dynamical tunneling [55]. Our calculation therefore assumes a high ground-state preparation fidelity followed by an adiabatic transport.

Using the formalism developed in Refs. [56,57], we evaluate now the heating of the atomic cloud due to fluctuations of the different experimental parameters such as laser stability (polarization, power, pointing) and surface position (both angle and absolute position).

We consider here a 1D problem where the different noises on each experimental parameters are uncorrelated and the time dependence of the QHO parameters (ϵ_k, ϵ_z) is treated independently. For noises affecting both the trap center position and trap frequencies, each heating term is calculated independently and compared. The independence hypothesis is valid when the corresponding heating times are separated by several orders of magnitude, which is the case for the data presented below. Out of the experimental parameters, we present below only the contributions of the most critical parameter: the angular positioning of the chip, driven by the motor. The 1D hypothesis is justified in this case since only ν_z is significantly affected and because it induces heating over the shortest timescale. The total heating rate can be generalized to higher dimensions as the average of the ones obtained by treating each spatial dimension separately ([39], Sec. 3.1.4.1.).

Following Refs. [56,57], we consider the Hamiltonian of the form

$$H(t) = \tfrac{1}{2}m\omega_z^2(1 + \epsilon_k(t))(z - \epsilon_z(t))^2, \tag{8}$$

where ϵ_k (resp. ϵ_z) is the fractional fluctuation in the spring constant (resp. trap center position) studied using perturbation theory.

Fluctuations on the spring constant lead to an exponential increase of the average energy with a constant rate Γ_k:

$$\Gamma_k = \frac{1}{\tau_k} = \pi^2\nu_z^2 S_k(2\nu_z), \tag{9}$$

where ν_z is the trap frequency and S_k is the one-sided power spectrum of the fractional fluctuation in the spring constant normalized, so that

$$\int_0^\infty S_k(\nu_z) = \epsilon_{0,k}^2, \tag{10}$$

with $\epsilon_{0,k}$ the root-mean-square fractional fluctuation in the spring constant.

Fluctuations on the trap center position lead to a heating rate independent of the trap energy. We define an energy doubling time τ_z as the time needed to double the initial average energy:

$$\tau_z = \frac{\langle E_z(t=0)\rangle}{4m\pi^4\nu_z^4 S_z(\nu_z)}, \tag{11}$$

where $\langle E_z(t=0)\rangle$ is the initial average energy, m is the particle mass, and S_z is the one-sided power spectrum of the fractional fluctuation in the trap center position.

Fluctuations in the incidence angle lead to fluctuations in both the trap frequency and position:

$$\begin{aligned} \epsilon_k(\theta) &= 2\delta\theta\ \tan(\theta), \\ \epsilon_z(\theta) &= \delta\theta\ z_0(\theta)\tan(\theta), \end{aligned} \tag{12}$$

with $\delta\theta$ the angle fluctuations and $z_0(\theta)$ the distance to the surface defined in Eq. (2).

Because the energy increase from ϵ_k is the dominating one at a constant time, we show only the results of the study of ϵ_k. Extra care is required during the initial stage of the transport due to the dependence in $\tan(\theta)$, which diverges for grazing incidence.

We considered two distinct types of motors, one piezo-driven stepper motor [58] and a continuous rotation motor [59].

We plot in Fig. 4(b) the two heating times for both these motors as a function of the trap frequency, computed using Eqs. (9) and (12). The stepper motor (gray curve) is globally more noisy and presents problematic harmonics at half the drive frequency (1 kHz), which would constraint the experiment. The noise spectrum of the WLG-75 sets an upper bound on the energy increase over the 100 ms long transport of a cloud with a maximum trap frequency of 20 kHz (E_0/h) as $\Delta E/h = E_0/h(e^{\Gamma t} - 1) < 10^{-4} \times 20\,\text{kHz}$. This contribution is below the theoretical heating due to the scattering of photons from the dipole trap laser field [41] $\Delta E_{\text{DT}}/h = 3 \times 10^{-3} \times 2\,\text{kHz}$. Both lead to a negligible energy increase: $\Delta E/E_0 = 3 \times 10^{-4} \ll 1$ and the limitation of the lifetime by noise-induced heating and photon scattering can therefore be disregarded.

In addition, for typical parameters, the tunneling time for the first excited state is 100 times shorter than for the ground state. Extracting the timescale of the exponentially decaying lifetime naturally rejects short-time errors so a small population in the excited state will simply appear as a reduction of the initial atom number and will not significantly impact the computed lifetime, nor the extracted value of c_4.

Adsorbate induced and patch electric fields. A spurious electrostatic effect arises from atoms adsorbed on the surface acting as electric dipoles (with moment $\mu_{\text{ads}} = 3.2$ D [11]) and interacting with the atomic sample. In Ref. [14], it was shown that the measurement of this effect at longer distances could be used to infer its contribution at short distances. To further mitigate this effect, the number of adsorbed atoms can be reduced or even removed by heating the surface [11]. Following Ref. [60], we consider a Gaussian distribution with $N_{\text{ads}} = 10^9$ Rb atoms of size $\sigma_\mu = 100$ μm deposited on the surface around (x_0, y_0). The electric potential at (x_0, y_0) is given along z by

$$E_{\text{ads}} = N_{\text{ads}}\mu_{\text{ads}} \frac{\sqrt{2\pi}\left(z^2 + \sigma_\mu^2\right)\text{erfcx}\left(\frac{z}{\sqrt{2}\sigma_\mu}\right) - 2z\sigma_\mu}{8\pi\epsilon_0\sigma_\mu^5}, \quad (13)$$

with $\text{erfcx}(\text{x}) = \text{e}^{\text{x}^2}(1 - \text{erf}(\text{x}))$ and ϵ_0 the vacuum electric permeability. The generated potential is then $U_{\text{ads}} = -\alpha_0/2|E_{\text{ads}}|^2$, with α_0 the atomic polarizability of the ground state. This effect induces a maximum relative error on the tunneling time $\delta\tau/\tau = 10^{-3}$ and thus contributes to the error budget at the level of $\epsilon_\tau = 10^{-4}$.

The effect of patch electric fields [61] on metallic reflecting surfaces can be mitigated by using strongly grounded plane surfaces.

Background losses. Collisions with high energy background atoms are another source of trap losses. The loss coefficient for collisions with ground-state ^{87}Rb atoms depends on the background gas and we consider the highest value for common gases [62] $\gamma_i/P = 3.75 \times 10^7$ mbar^{-1}s^{-1}. A pressure of 10^{-9} mbar, routinely achieved in cold-atom experiments, gives a lifetime of 26 s. At such a pressure, the contribution of background loss on the error on c_4 will decrease with the tunneling time considered and, for $\tau_t = 100$ ms, this relative error is upper bounded to $\epsilon_\tau = \frac{\partial c_4^n}{\partial \tau}\frac{\tau}{c_4}\frac{\delta\tau}{\tau} < 0.1\frac{\delta\tau}{\tau} = 3.75 \times 10^{-4}$. This effect is thus negligible at first order. If necessary, it could be calibrated far from the surface and subtracted from the lifetime measurement.

Complex refractive index uncertainty. An error on the refractive index induces an error on the simulated optical potential, and thus on the c_4 measurement. Defining the refractive index as $n = \tilde{n} - \kappa i$, the dominant contribution comes from the error on the extinction coefficient κ that modifies the skin depth and displaces the first fringe. For thin gold films [48,63] with a thickness of 20–120 nm, $\kappa \in [6.99, 7.31]$. For the parameters of Fig. 3(c) and $\tau_t > 1$ ms, this induces an error $\delta\tau/\tau < 0.13$ so it contributes to the error budget for $\epsilon_\tau < 10^{-2}$. Surface temperature also affects κ. According to Ref. [64], a temperature variation from 23 to 100 °C induces only a 1% variation on κ so a relative error $\epsilon_\tau < 3 \times 10^{-3}$. This effect is negligible given that with the atom chip configuration we proposed, we experimentally measured a maximum temperature increase of 10 °C after continuously seeding 24 A (electrical power of 172 W) for 20 s. Typical gold mirrors have a reflectivity above 96% at 1064 nm. Even at an optical power of 5 W, the absorbed power $P_{\text{abs}} = 0.2\,\text{W}$ would be negligible compared to the dissipated electrical power.

Johnson-noise-induced spin flips. Theory [65,66] and experiments [35,67,68] indicate that radio frequency spin flip transitions occur when atoms are magnetically trapped close to metallic and dielectric surfaces due to thermal fluctuations of electrons. For distances between 500 nm–1 μm, CP forces are the dominant effect [35] and the spin flip lifetime is given by [66]

$$\tau_{\text{flip}} = \left(\frac{8}{3}\right)^2 \frac{\tau_0}{\bar{n}_{\text{th}} + 1}\left(\frac{\omega}{c}\right)^3 \frac{\delta^2 z_0^2}{2h}, \quad (14)$$

where τ_0 is the lifetime in free space at zero temperature, $\bar{n}_{\text{th}}$ is the mean number of thermal photons per mode at the frequency ω of the spin flip, $\delta \approx 100$ μm the skin depth for Au, and h the film thickness. At a transition frequency $\omega/2\pi = 500\,\text{kHz}$ (typical for magnetically trapped atoms on an atom chip [35]) and temperature of 400 K, $\tau_0/(\bar{n}_{\text{th}} + 1) = 4 \times 10^{18}$ s. For a cloud at $z_0 = 1$ μm, and a surface thickness $h = 100$ nm, we compute $\tau_{\text{flip}} = 1\,\text{s} > \tau_t$. If this effect becomes critical, we emphasize that our method also allows for a pure optical dipole trap configuration. Indeed, the magnetic trap can be fully turned off, which suppress the contribution of this effect. In the present configuration, the measurement can be done for final distances under 600 nm, and the transport requires a transient increased optical power. However, we proposed to rotate the surface only because it is experimentally easier. To reach the entire range of distances of Fig. 1(d), another solution is to rotate the beam with a fixed surface, perpendicular to gravity.

TABLE I. List of the errors impacting the c_4 measurement.

Effect	Uncertainty	$\delta c_4/c_4^n$
Optical power (P)	$\delta P/P = 6 \times 10^{-2}$	$\epsilon_P < 10^{-1}$
Lifetime measurement (τ)	$\delta\tau/\tau = 0.1$	$\epsilon_\tau = 10^{-2}$
Johnson noise	$\tau_{\text{flip}} = 1$ s	$\epsilon_\tau = 10^{-2}$
Refractive index (n)	$\kappa \in [6.99, 7.31]$	$\epsilon_\tau < 10^{-2}$
Surface angle (θ)	$\delta\theta = 423$ µrad	$\epsilon_\theta < 10^{-3}$
Background losses	$\tau = 26$ s	$\epsilon_\tau = 3.75 \times 10^{-4}$
Wire current	$\delta I_Z = 10$ mA	$\epsilon_\theta < 2 \times 10^{-4}$
Adsorbate fields	$\delta\tau/\tau = 10^{-3}$	$\epsilon_\tau = 10^{-4}$
Total		$<10^{-1}$

V. CONCLUSION AND OUTLOOK

In this paper, we showed that using a reflected optical dipole trap on a rotating atom chip allows to precisely measure the CP coefficient of a reflecting surface. This is achieved by measuring atom losses induced by the distance-dependent tunneling through the potential barrier toward the surface. By rotating the surface, it is possible to probe the interaction at various distances and could be used to verify the $1/z^\alpha$ scaling law (c_4 being independent of z), and potentially probe the transition from the CP (retarded) to the Lennard-Jones regime. We present in Table I the contributions from different systematic effects showing that a relative uncertainty of $\delta c_4/c_4 = 0.1$ can be achieved and could be reduced to a few percent with efforts on the calibration of the optical power and by optimizing (P, θ) to minimize the sensitivities introduced in Eq. (7) for a target c_4.

Other measurement techniques of the atom-surface interaction can also be implemented using our scheme, for example, by measuring the modification of the trap frequency due to the CP force [13]. This frequency could be extracted by measuring the oscillation frequency of the center of mass of the cloud or by measuring the lifetime after exciting a parametric oscillation, or even transfering the cloud to a higher vibrational state with a significantly shorter tunneling time. In our trapping potential, we estimate a normalized oscillation frequency shift on the order of 10^{-2}, well above the 10^{-4} reported in Ref. [13], where the effect was already within experimental measurement precision.

The determination of the c_4 coefficient depends on the precise knowledge of the total trapping potential. Out of the four effects involved in Eq. (3), the dipole force is the main source of error. Indeed, gravity and the magnetic potential can be precisely simulated for a correctly defined geometry of the trapping wires and coils structures. The exact magnetic field can also be measured via microwave spectroscopy. To go beyond the numerical model we implemented, the light shift due to the laser field could be computed by diagonalizing the Hamiltonian $H = H_{\text{Stark}} + H_{\text{hf}}$ composed of the sum of the ac Stark Hamiltonian and the hyperfine shift Hamiltonian. Such a diagonalization leads to relative corrections on U_{opt} that are typically below 10^{-4}.

The atom-surface interaction primarily depends on the atom-surface distance, but also on the surface and environment properties. At distances on the order of the thermal wavelength (typically a few micrometers), thermal fluctuations from the surface and its environment contribute to the Casimir-Polder force [11,69].

The rotation transport method introduced in this paper is therefore suitable to precisely and locally measure atom-surface interaction over a large range of distances.

ACKNOWLEDGMENTS

This work was supported by the Investments for the Future Programme IdEx Bordeaux-LAPHIA (ANR-10-IDEX-03-02), ANR contracts (JCJC ANR-18-CE47-0001-01 and QUANTERA21 ANR-22-QUA2-0003), and the Quantum Matter Bordeaux. R.V. acknowledges financial support from the European Union through "NextGenerationEU/PRTR" (Grant No. FJC2021-047840-I) and "Severo Ochoa" Center of Excellence CEX2019-000910-S; Generalitat de Catalunya through the CERCA program, DURSI Grant No. 2021 SGR 01453 and QSENSE (GOV/51/2022); Fundació Privada Cellex; and Fundació Mir-Puig.

DATA AVAILABILITY

There are no publicly available research data or software supporting this manuscript. Requests for further information or data should be sent to the authors.

APPENDIX A: PARAMETER SCANS

In this Appendix, we present a generic method to circumvent systematic errors by scanning an experimental parameter. We do so, without loss of generality, on a randomly chosen test case. The experimental conditions of this scan should be tailored to each expected value of c_4 and we do not derive here any general results.

We show that a systematic error on a parameter, here P, is not equivalent to an error on c_4. We define sets of 1D numerical curves at fixed angle: $\tau_{c_4} = \tau_{c_4}(P)$. If a systematic error on P was equivalent to one on c_4, a curve $\tau_{c_4}^{(1)}(P)$ could match another curve $\tau_{c_4}^{(2)}(P)$ for two values of c_4 by translating the x axis of one of them (i.e., corresponding to an absolute error on P, denoted as $\tilde{P}$).

As an example, we consider a measurement of the lifetime at a fixed angle for two optical powers $P_1 = 1.255$ W and $P_2 = 0.72$ W. Numerically, for a single measurement of the lifetime at P_1, we cannot discriminate between an absolute error $\tilde{P}$ on P_1 and an error on c_4. In other words, for two values $c_4^{(1)} = 2.4 \times 10^{-55}$ J m^4 and $c_4^{(2)} = 2.5 \times 10^{-55}$ J m^4, there exist $\tilde{P}_0$ so that $\tau_{c_4^{(1)}}(P_1) = \tau_{c_4^{(2)}}(P_1 + \tilde{P}_0)$. However, at P_2, the corresponding tunneling time is no more equal and computed to be $\tau_{c_4^{(1)}}(P_2) = 0.84$ ms and $\tau_{c_4^{(2)}}(P_2 + \tilde{P}_0) = 0.75$ ms. Here, a 4% difference on c_4 is discriminated, given an uncertainty on the lifetime measurement under 10% for two values of power separated by 40%. This shows that both uncertainties are not equivalent. This method allows to circumvent systematic errors on the optical power (or the surface angle). Thus, increasing the number of measurements (statistically or including other powers) obviously relaxes the constraint on the lifetime precision and allows to extend the parameter range in which this method applies [$\tau_{c_4}(P)$ curves are not linear and, in some cases, cross at more than one point]. In practice, this method is implemented by fitting the experimental data with a numerical curve $\tau_{c_4}(P+\tilde{P})$ using two free parameters: $(c_4, \tilde{P})$.

APPENDIX B: MONTE CARLO SIMULATION

In this Appendix, we compare the uncertainty previously established in the paper with a Monte Carlo simulation on a randomly chosen test case. We show that the error budget established in Sec. IV is equal to one derived using Monte Carlo simulation, which validates Eq. (7). Systematic errors are the main contributions to this error budget, summarized in Table I, and the statistical fluctuations expected on each parameter are small, yielding a relative standard deviation of the lifetime in the 10% range. To perform Monte Carlo simulations, we generate for each parameter $N_e = 2\times 10^3$ random values from Gaussian distributions with mean value μ and standard deviation σ. We study the relative standard deviation of the computed lifetime σ_τ/μ_τ, for three angles ($\theta = [60, 55, 50]^\circ$). For a power distribution with ($\mu = 1\mathrm{W}, \sigma/\mu = 0.05$) and a fixed c_4, we compute $\sigma_\tau/\mu_\tau = [0.89(1), 0.65(1), 0.64(1)]$. For a fixed power and a c_4 distribution with ($\mu = 2.1\times 10^{-55}\mathrm{J\,m^4}, \sigma/\mu = 0.07$), $\sigma_\tau/\mu_\tau = [0.73(1), 0.71(1), 0.84(1)]$. Dividing the standard deviation of each parameter by 2 reduces σ_τ by the same factor, confirming the validity of the linear approximation of the fluctuations. The composite relative standard deviation including both fluctuating parameters is $\sigma_\tau/\mu_\tau = [1.28(2), 1.02(2), 1.05(3)]$. This is equal to the root mean square of each independent contribution $[1.15(2), 0.96(1), 1.06(2)]$. This confirms that in this regime, the error contribution from each parameter can be linearized: A relative standard deviation on P of 5% is equivalent (i.e., will induce the same uncertainty on τ) to one on c_4 of 7%. Thus, the variational approach implemented in the rest of the article is valid. We observe that the scaling with θ for both contributions is different. Thus, as discussed in Appendix A, scanning parameters could increase the precision on the measurement.

[1] L. Amico *et al.*, Roadmap on atomtronics: State of the art and perspective, AVS Quantum Sci. **3**, 039201 (2021).

[2] M. Gullans, T. G. Tiecke, D. E. Chang, J. Feist, J. D. Thompson, J. I. Cirac, P. Zoller, and M. D. Lukin, Nanoplasmonic lattices for ultracold atoms, Phys. Rev. Lett. **109**, 235309 (2012).

[3] J. D. Hood *et al.*, Atom-atom interactions around the band edge of a photonic crystal waveguide, Proc. Natl. Acad. Sci. USA **113**, 10507 (2016).

[4] J. S. Douglas *et al.*, Quantum many-body models with cold atoms coupled to photonic crystals, Nat. Photonics **9**, 326 (2015).

[5] F. London, Zur Theorie und systematik der molekularkrafte, Z. Phys. **63**, 245 (1930).

[6] J. E. Lennard-Jones, Processes of adsorption and diffusion on solid surfaces, Trans. Faraday Soc. **28**, 333 (1932).

[7] S. Y. Buhmann *et al.*, Impact of anisotropy on the interaction of an atom with a one-dimensional nano-grating, Int. J. Mod. Phys. A **31**, 1641029 (2016).

[8] P. Barcellona *et al.*, Van der Waals interactions between excited atoms in generic environments, Phys. Rev. A **94**, 012705 (2016).

[9] C. Abbas *et al.*, Strong thermal and electrostatic manipulation of the Casimir force in graphene multilayers, Phys. Rev. Lett. **118**, 126101 (2017).

[10] P.-P. Crépin *et al.*, Casimir-Polder shifts on quantum levitation states, Phys. Rev. A **95**, 032501 (2017).

[11] J. M. Obrecht *et al.*, Measurement of the temperature dependence of the Casimir-Polder force, Phys. Rev. Lett. **98**, 063201 (2007).

[12] H. B. G. Casimir and D. Polder, The influence of retardation on the London-van der Waals forces, Phys. Rev. **73**, 360 (1948).

[13] D. M. Harber *et al.*, Measurement of the Casimir-Polder force through center-of-mass oscillations of a Bose-Einstein condensate, Phys. Rev. A **72**, 033610 (2005).

[14] Y. Balland *et al.*, Quectonewton local force sensor, Phys. Rev. Lett. **133**, 113403 (2024).

[15] A. Landragin *et al.*, Measurement of the van der Waals force in an atomic mirror, Phys. Rev. Lett. **77**, 1464 (1996).

[16] T. A. Pasquini *et al.*, Quantum reflection from a solid surface at normal incidence, Phys. Rev. Lett. **93**, 223201 (2004).

[17] C. Stehle *et al.*, Plasmonically tailored micropotentials for ultracold atoms, Nat. Photonics **5**, 494 (2011).

[18] H. Bender *et al.*, Probing atom-surface interactions by diffraction of Bose-Einstein condensates, Phys. Rev. X **4**, 011029 (2014).

[19] C. I. Sukenik *et al.*, Measurement of the Casimir-Polder force, Phys. Rev. Lett. **70**, 560 (1993).

[20] J. Morley *et al.*, Characterising a tunable, pulsed atomic beam using matter-wave interferometry, J. Phys. B: At. Mol. Opt. Phys. **54**, 155301 (2021).

[21] C. Garcion *et al.*, Intermediate-range Casimir-Polder interaction probed by high-order slow atom diffraction, Phys. Rev. Lett. **127**, 170402 (2021).

[22] J. Lecoffre *et al.*, Measurement of Casimir-Polder interaction for slow atoms through a material grating, Phys. Rev. Res. **7**, 013232 (2025).

[23] A. P. Mosk *et al.*, Optical excitation of atomic hydrogen bound to the surface of liquid helium, Phys. Rev. Lett. **81**, 4440 (1998).

[24] M. Oria *et al.*, Spectral observation of surface-induced van der Waals attraction on atomic vapour, Europhys. Lett. **14**, 527 (1991).

[25] M. Fichet *et al.*, Exploring the van der Waals atom-surface attraction in the nanometric range, Europhys. Lett. **77**, 54001 (2007).

[26] Whittaker *et al.*, Optical response of gas-phase atoms at less than $\lambda/80$ from a dielectric surface, Phys. Rev. Lett. **112**, 253201 (2014).

[27] R. Folman *et al.*, Controlling cold atoms using nanofabricated surfaces: Atom chips, Phys. Rev. Lett. **84**, 4749 (2000).

[28] J. Reichel *et al.*, Microchip traps and Bose–Einstein condensation, Appl. Phys. B **74**, 469 (2002).

[29] T. L. Gustavson *et al.*, Transport of Bose-Einstein condensates with optical tweezers, Phys. Rev. Lett. **88**, 020401 (2001).

[30] J. Trisnadi *et al.*, Design and construction of a quantum matter synthesizer, Rev. Sci. Instrum. **93**, 083203 (2022).

[31] J. I. Gillen *et al.*, Two-dimensional quantum gas in a hybrid surface trap Phys. Rev. A **80**, 021602(R) (2009).

[32] P. Treutlein *et al.*, Coherence in microchip traps, Phys. Rev. Lett. **92**, 203005 (2004).

[33] D. E. Chang *et al.*, Trapping atoms using nanoscale quantum vacuum forces, Nat. Commun. **5**, 4343 (2014).

[34] M. Bellouvet *et al.*, Doubly dressed states for near-field trapping and subwavelength lattice structuring, Phys. Rev. A **98**, 023429 (2018).

[35] Y.-J. Lin, I. Teper, C. Chin, and V. Vuletić, Impact of the Casimir-Polder potential and Johnson noise on Bose-Einstein condensate stability near surfaces, Phys. Rev. Lett. **92**, 050404 (2004).

[36] P. G. Petrov *et al.*, Trapping cold atoms using surface-grown carbon nanotubes, Phys. Rev. A **79**, 043403 (2009).

[37] R. Salem *et al.*, Nanowire atomchip traps for sub-micron atom–surface distances, New J. Phys. **12**, 023039 (2010).

[38] W. Hänsel *et al.*, Bose–Einstein condensation on a microelectronic chip, Nature (London) **413**, 498 (2001).

[39] J.-B. Gerent, Transport and coupling of ultra-cold atoms to nano-structured surfaces, PhD. thesis, Université de Bordeaux, 2024.

[40] S. J. Orfanidis, Electromagnetic waves and antennas, (1999–2016), https://ece.rutgers.edu/orfanidis.

[41] R. Grimm, M. Weidemüller, and Y. B. Ovchinnikov, *Optical Dipole Traps for Neutral Atoms*, Advances In Atomic, Molecular, and Optical Physics, Vol. 42, edited by B. Bederson and H. Walther (Academic Press, 2000), pp. 95–170.

[42] M. Bellouvet, Condensation de Bose-Einstein et simulation d'une méthode de piégeage d'atomes froids dans des potentiels sublongueur d'onde en champ proche d'une surface nanostructurée, Ph.D. thesis, Université de Bordeaux, 2018.

[43] J. Berroir *et al.*, Nanotrappy: An open-source versatile package for cold-atom trapping close to nanostructures, Phys. Rev. Res. **4**, 013079 (2022).

[44] A. Bouscal, Slow-mode nanophotonics and cold atoms: Towards a versatile waveguide QED platform, PhD. thesis, Sorbonne Université, 2024.

[45] H. Friedrich *et al.*, Quantum reflection by Casimir–van der Waals potential tails, Phys. Rev. A **65**, 032902 (2002).

[46] N. P. Stern *et al.*, Simulations of atomic trajectories near a dielectric surface, New J. Phys. **13**, 085004 (2011).

[47] A. Aspect and J. Dalibard, Measurement of the atom-wall interaction: From London to Casimir-Polder, in *Poincaré Seminar 2002*, edited by B. Duplantier and V. Rivasseau (Birkhäuser Basel, Basel, 2003).

[48] D. Yakubovsky *et al.*, Optical constants and structural properties of thin gold films, Opt. Express **25**, 25574 (2017).

[49] D. J. Griffiths and D. F. Schroeter, *Introduction* to *Quantum Mechanics* (Cambridge University Press, Cambridge, 2018), 3rd ed.

[50] ThorlabsS120C, https://www.thorlabs.com/item/s120c.

[51] L. P. Pitaevskii, Dynamics of collapse of a confined Bose gas, Phys. Lett. A **221**, 14 (1996).

[52] NIST calibration services, https://shop.nist.gov/ccrz__ProductDetails?sku=42110C&cclcl=en_US, accessed 13 July 2026.

[53] J. Hadler *et al.*, NIST measurement services, https://nvlpubs.nist.gov/nistpubs/Legacy/SP/nistspecialpublication250-75.pdf.

[54] E. A. Burt *et al.*, Coherence, correlations, and collisions: What one learns about Bose-Einstein condensates from their decay, Phys. Rev. Lett. **79**, 337 (1997).

[55] M. J. Davis and E. J. Heller, Quantum dynamical tunneling in bound states, J. Chem. Phys. **75**, 246 (1981).

[56] T. A. Savard *et al.*, Laser-noise-induced heating in far-off resonance optical traps, Phys. Rev. A **56**, R1095 (1997).

[57] M. E. Gehm *et al.*, Dynamics of noise-induced heating in atom traps, Phys. Rev. A **58**, 3914 (1998).

[58] New Focus picomotor 8321, https://www.newport.com/p/8321.

[59] Tekceleo WLG-75, https://www.tekceleo.com/wlg-75-r-motor/.

[60] Y. Balland, Mesure des interactions atomes-surface avec un capteur quantique à atomes froids, Thèse de doctorat, Sorbonne université, 2024.

[61] O. Cherry, J. D. Carter, and J. D. D. Martin, Fabrication of an atom chip for Rydberg atom-metal surface interaction studies, arXiv:2510.11902.

[62] T. Arpornthip, C. A. Sackett, and K. J. Hughes, Vacuum-pressure measurement using a magneto-optical trap, Phys. Rev. A **85**, 033420 (2012).

[63] G. Rosenblatt *et al.*, Nonmodal plasmonics: Controlling the forced optical response of nanostructures, Phys. Rev. X **10**, 011071 (2020).

[64] H. Reddy *et al.*, Temperature-dependent optical properties of gold thin films, Opt. Mater. Express **6**, 2776 (2016).

[65] P. K. Rekdal *et al.*, Thermal spin flips in atom chips, Phys. Rev. A **70**, 013811 (2004).

[66] S. Scheel *et al.*, Atomic spin decoherence near conducting and superconducting films, Phys. Rev. A **72**, 042901 (2005).

[67] D. M. Harber *et al.*, Thermally induced losses in ultra-cold atoms magnetically trapped near room-temperature surfaces, J. Low Temp. Phys. **133**, 229 (2003).

[68] M. P. A. Jones *et al.*, Spin coupling between cold atoms and the thermal fluctuations of a metal surface, Phys. Rev. Lett. **91**, 080401 (2003).

[69] M. Antezza *et al.*, New asymptotic behavior of the surface-atom force out of thermal equilibrium, Phys. Rev. Lett. **95**, 113202 (2005).